Equation of state, phonons, and lattice stability of ultrafast warm dense matter

L. Harbour,[1] M. W. C. Dharma-wardana,[2] D. D. Klug,[2] and L. J. Lewis[1]

[1]*Département de Physique and Regroupement Québécois sur les Matériaux de Pointe, Université de Montréal,
C.P. 6128, Succursale Centre-Ville, Montréal, Québec, Canada H3C 3J7*

[2]*National Research Council of Canada, Ottawa, Ontario, Canada K1A 0R6*

Using the two-temperature model for ultrafast matter (UFM), we compare the equation of state, pair-distribution functions $g(r)$, and phonons using the neutral pseudoatom (NPA) model with results from density functional theory (DFT) codes and molecular dynamics (MD) simulations for Al, Li, and Na. The NPA approach uses state-dependent first-principles pseudopotentials from an "all-electron" DFT calculation with finite-T exchange-correlation functional (XCF). It provides pair potentials, structure factors, the "bound" and "free" states, as well as a mean ionization $\bar{Z}$ unambiguously. These are not easily accessible *via* DFT+MD calculations which become prohibitive for T/T_F exceeding $\sim$0.6, where T_F is the Fermi temperature. Hence, both DFT+MD and NPA methods can be compared up to $\sim$8 eV, while higher T can be addressed *via* the NPA. The high-T_e phonon calculations raise the question of UFM lattice stability and surface ablation in thin UFM samples. The ablation forces in a UFM slab are used to define an "ablation time" competing with phonon formation times in thin UFM samples. Excellent agreement for all properties is found between NPA and standard DFT codes, even for Li where a strongly nonlocal pseudopotential is used in DFT codes. The need to use pseudopotentials appropriate to the ionization state $\bar{Z}$ is emphasized. The effect of finite-T XCF is illustrated via its effect on the pressure and the electron-density distribution at a nucleus.

I. INTRODUCTION

The equation of state (EOS) of common thermodynamic phases of matter is well understood. However, recent laser and shock-wave experiments have accessed novel ultrafast regimes of density and temperature which are of great theoretical and technological interest. The same physics appears during the injection of hot carriers in field-effect transistors and other nanostructures. Topics such as inertial-confinement fusion [1], Coulomb explosions [2], space reentry shielding, laser machining, and ablation [3] involve such regimes of warm dense matter (WDM). However, elementary approaches cannot be applied since the Coulomb coupling constant Γ, i.e., the ratio of the Coulomb energy to the kinetic energy, is larger than unity. The electrons may range from degenerate to Boltzmann type, with $T/E_F \sim 1$ or larger, where T is electron temperature in energy units, while E_F is the Fermi energy. This causes a prohibitive increase in basis sets that span the many excited electronic states. WDMs pose a theoretical challenge for rapid accurate computations of properties such as pressure, heat capacity, phonons, and conductance needed even for equilibrium WDMs.

A class of WDMs known as ultrafast matter (UFM) is produced when energy is deposited using an ultrafast pulsed laser on a metal surface [4]. The light couples strongly to the mobile electrons which equilibrate on femtosecond time scales, to a temperature T_e (as high as many eV) while the much heavier ions and their strongly bound core electrons remain essentially at their initial temperature T_i, i.e., usually the room temperature T_r. This two-temperature WDM (2T-WDM) phase with $T_e > T_i$ remains valid for time scales t such that $\tau_{ee} < \tau_{ii} < t < \tau_{ei}$, where τ_{ee}, τ_{ii}, and τ_{ei} are the electron-electron, ion-ion, and electron-ion temperature relaxation times, respectively. It has been shown for near-solid densities that τ_{ei} is of the order of picoseconds,

and orders of magnitude longer than τ_{ee} and τ_{ii} [5,6]. For WDMs with $\theta = T/E_F$ small, similar relaxation times hold as seen in calculations for typical systems [7]. Experiments using femtosecond pump-probe techniques [8,9] provide data for quasiequilibrium analogs of free energy and pressure, transport, and relaxation processes. While many UFM samples do not conform to the 2T model (e.g., as in Medvadev *et al.* [10]), the 2T model provides a great simplification when it holds. Even for UFMs, theory and experiment are quite challenging as the system transits rapidly from a solid to a plasma depending on the pump energy. Hence, a theoretical model that encompasses a wide range of material conditions is needed to describe the time evolving system as a series of static 2T systems. The "quasiequilibrium" theory is applied to each static picture of the time evolving system.

In this work, we use the neutral pseudoatom (NPA) model, in the form given by Perrot and Dharma-wardana [11–16], to study the 2T-WDM regime of a few nominally *simple metals*, viz., aluminum, lithium, and sodium. These are "simple" at ambient conditions since their valence electrons are "free-electron like" and energetically separated from the core electrons. The number $\bar{Z}$ of valence electrons per atom (mean ionization) for Al, Li, and Na is 3, 1, and 1, respectively. Furthermore, if the matter density is ρ, each ion can be assigned a spherical volume with the Wigner-Seitz (WS) radius $r_{WS} = (3/4\pi\rho)^{1/3}$, and it can be shown for Al, Li, Na that the bound-electron core has a radius r_c such that it is well inside the WS sphere for the temperatures studied here (see Sec. IV D). In such cases, the definition of $\bar{Z} = N - n_b$, where n_b is the number of bound electrons in the core, is unambiguous, clear, and is a physically measurable quantity, e.g., using x-ray Thomson scattering [17]. In the case of equilibrium WDM, the NPA calculated $\bar{Z}$ for Al and Li remains 3 and 1 in the range $0 < T_e < 8$ eV whereas in the case of sodium, $\bar{Z}$ rises to 1.494 by $T = 8$ eV and 1.786 by 10 eV. The case of

Na provides us an example of a typical variation of $\bar{Z}$ very common in equilibrium WDM systems and handled without any ambiguity and with thermodynamic consistency by the NPA approach coupled with determinations of the ion-ion $g(r)$ using the NPA pair potentials. However, in the case of UFM, which is the scope of this work, $\bar{Z}$ is kept unchanged for all three elements through the $0 < T_e < 8$ eV temperature range.

The NPA model replaces the interacting *many-nuclear* and *many-electron* problem by an effective noninteracting *single-nuclear* and *single-electron* formulation where the many-body problem is reduced using finite-T density functional theory (DFT) [18,19]. The NPA charge densities are used to construct $2T$ pseudopotentials and effective ion-ion pair potentials. The method takes into account particle correlations at the pair-density level and beyond using density functional methods via exchange-correlation functionals for electrons, and ion-correlation functionals for ions in a decoupled step which uses a classical integral equation or molecular dynamics. The NPA framework is well adapted to treating metallic systems ranging from solids to liquids or plasmas at very high or low compressions, and from $T = 0$ to several keV. The importance and relevance of the NPA lies in its accuracy, flexibility, and computational rapidity compared to DFT coupled to molecular dynamics (MD) methods (DFT+MD). However, the NPA, as used here, is inapplicable when inner-shell electrons (e.g., d electrons) play a role in the ion-ion interactions (e.g., as in transition metals). A simple metal becomes "complex" when its electronic bound states extend beyond its WS radius r_{WS}. This is not a shortcoming but a strength of the model which signals the need for multi-ion contributions into the theory in such ranges of temperature and pressure. In such regimes, discontinuities in $\bar{Z}$ where some are spurious may appear unless suitable electron-ion XC-correlation potentials are included in the theory [20]. Furthermore, *transient* molecule formation can be successfully handled [21] within the NPA as it allows for binary ion-ion correlations.

We compare our $2T$-NPA predictions with those from solid-state DFT electronic-structure codes such as ABINIT [22] and VASP [23], which use MD to evolve the finite-T ionic structures. These codes are primarily designed for $T_i = T_e = 0$ situations, and solve the *multinuclear* Kohn-Sham equations in a plane-wave basis, using $T = 0$ pseudopotentials to reduce the number of electrons needed in the simulations. The solid, liquid, or plasma is treated as a *periodic solid* in a simulation box ("supercell") containing N nuclei, with N being $\sim$100. A finite-T_e Fermi-Dirac distribution for electron occupation numbers is used, along with $T = 0$ pseudopotentials and $T = 0$ exchange-correlation functionals (XCF). The number of electronic bands required to access high T_e increases rapidly with T_e and becomes prohibitive for T_e/E_F greater than $\sim$1. This method generates energy bands for the periodic solid where as in reality there are *no such band structures* in liquids and plasmas. This artifact is overcome by generating electronic-structure calculations for many static ionic configurations via MD simulations and averaging over a large number of them.

DFT+MD provides only a "mean ionization" for the whole N-ion supercell; it cannot provide, e.g., the composition of an equilibrium mixture of specific charge states of ions in a C, H "plastic" at, say, 1 eV. Furthermore, VASP and ABINIT

currently only implement the zero-T XCF even though finite-T parametrizations have been available for some time, e.g., the evaluation of finite-T bubble diagrams [24,25], from the work of Iyetomi and Ichimaru [26], Perrot and Dharma-wardana (PDW) [27], and from Feynman-path methods by Brown *et al.* [28] parametrized recently by Karasiev *et al.* [29]. The present NPA calculations are done with the PDW finite-T XCF which is in close agreement with the quantum simulations of Brown *et al.* [30]. In most cases, finite-T XC effects contribute only small corrections and DFT+MD provides valuable benchmarks for testing other methods.

The NPA method is summarized in Sec. II where we emphasize its application to the $2T$ regime. Resulting $2T$ pair potentials ($2T$PP), quasiequilibrium phonon dispersions, and pair-distribution functions (PDF) $g(r)$ are presented in Sec. III. The phonon calculations confirm the results and also validate the meV accuracy of the NPA method. The NPA $g(r)$ calculations for normal and compressed Li ($\sim$ up to a compression of 2) show that the *local* pseudopotential for Li is successful. Here, we compare the ion-ion structure factor $S(k)$ with the simulations of Kietzmann *et al.* Having confirmed the accuracy of the pseudopotentials and pair potentials, the $2T$-thermodynamic properties, such as the quasipressure, are also presented. These are compared with the values for systems in thermal equilibrium. Discussions about phonon formation times in $2T$ systems, the role of finite-T XC contributions in the $2T$-EOS calculation, and the choice of suitable pseudopotentials in *ab initio* finite-T simulations are also presented.

II. NEUTRAL PSEUDOATOM MODEL

A. General description of the model

Several average-atom models and NPA models have been proposed, even in the early literature [31]. Many of these are intuitive cell models and are not true DFT models. A rigorous DFT formulation of a NPA model at $T = 0$ was first used for solids by Dagens [11,12]. There, the treatment of the ion distribution was developed in the traditional manner as providing a fixed external potential; Dagens showed that the NPA results at $T = 0$ agree closely with the band-structure codes available at the time. A finite-T version was given in several papers by Perrot [13] and Dharma-wardana [27,32,33]. In Ref. [32], the ion distribution $\rho(r)$ itself was treated within DFT using the property that the free energy $F[n,\rho]$ is a functional of *both* $n(r)$ and $\rho(r)$ simultaneously. A classical DFT equation for the ions and an ion-correlation functional $F_c^{ii}(\rho)$, approximated as a sum of hypernetted-chain (HNC) diagrams plus bridge diagrams, was introduced, *without* invoking a Born-Oppenheimer approximation or treating the ions as providing a fixed external potential [34]. Exchange-correlation functionals $F_{XC}^{ei}(\rho)$ for electron-ion interactions were also introduced although negligible in common materials. This puts the NPA approach on a very rigorous DFT footing where approximations enter in modeling the ion-correlation functional, just as in the case of the electron DFT problem for the electronic XCF.

However, in the following, we present the theory in terms of the more familiar superposition picture. We consider a system

of ions located at sites $\mathbf{R}_i$ at temperature T_i and average density ρ, interacting with a system of electrons at temperature T_e and average density n. The *multicenter* problem is reduced to a simplified *single-center* problem where the total electron density $n(r)$ is regarded as the superposition of single-site densities such that $n(r) = \sum_i n_i(r - \mathbf{R}_i)$. In contrast to ion-sphere (IS) models like those used in Purgatorio [35], or Piron and Blenski [36], Starrett and Saumon [37], the single-site free-electron density $n_f(r)$ extends over the whole of space, approximated by a correlation sphere [32] of radius R_c which is of the order of 10 ionic Wigner-Seitz radii. All particle correlations are assumed to have died out when $r \rightarrow R_c$. This R_c is similar to the linear dimension of the simulation box of a DFT+MD simulation which has to be as big as possible. However, in practice the charge distribution used in DFT+MD simulations spreads over a volume of about 100 ions. In contrast, the NPA correlation sphere with $R_c \simeq 10 r_{\mathrm{WS}}$ extends over $\{R_c/r_{\mathrm{WS}}\}^3$, i.e., the volume covered by $\sim$1000 ions. The calculation of course uses only one nucleus, but its charge density overlaps the space of some 1000 atoms, and this is crucial to getting the right pair potentials with long-range Friedel oscillations, and to satisfy the Friedel sum rule [32]. The IS models cannot satisfy the Friedel sum rule. At higher temperatures where particle correlations are weak, r_c may be reduced to, e.g., $5r_{\mathrm{WS}}$, but the results are independent of R_c, and R_c is *not* an optimization parameter.

The ion distribution $\rho(r) = \rho g_{ii}(r)$ contains the full ion-ion PDF, $g(r)$, when seen from any site taken as the origin. It is found that in most cases it is sufficient, as far as the bound-electron structure is concerned, to approximate $g(r)$ by a spherical cavity $c(r)$ of radius r_{WS} and total charge $\bar{Z}$ centered on the ion, followed by a uniform positive density ρ for $r > r_{\mathrm{WS}}$. As mentioned below, unlike in IS models, its effect will be subtracted out (as a "cavity correction") to obtain the response of a uniform electron gas to the nucleus. Thus, we have

$$c(r) = n[H(0) - H(r - r_{\mathrm{WS}})], \quad (1)$$

where $H(r)$ is the Heaviside step function. Initially $\bar{Z}$ is unknown but its value is obtained self-consistently from the iterative Kohn-Sham procedure. The single-site electron density is written as $n_i = \Delta n_i + m_i$ where m_i is the cavity correction and Δn_i is the electron pileup obtained by the DFT calculation for the electrons in the external potential V_{ext} given by

$$V_{\mathrm{ext}}(r) = -\frac{Z}{r} + \frac{1}{|\mathbf{r} - \mathbf{r}'|} \star c(\mathbf{r}'), \quad (2)$$

where the symbol $\star$ means integration over all space. Here, $Z = Z_n$ is the nuclear charge. The positive background with the WS cavity, the nucleus at its center, and the free-electron charge density filling the whole correlation sphere constitute the neutral pseudoatom [27,33]. The WDM system is made up of superpositions of such neutral pseudoatoms correlated to give the ion-ion $g(r)$, with the cavity contributions subtracted out.

For simple metallic systems, this cavity model that defines the extent of the bound states is sufficient to produce physically accurate results and is mathematically convenient, as shown in the papers by Dagens or those of Perrot and Dharma-wardana

cited above. Thus, to compute the cavity correction $m(r)$, we assume that the electrons respond linearly to the cavity $c(r)$, viz., in Fourier space,

$$m(q) = -V(q)c(q)\chi_{ee}(q,n,T_e). \quad (3)$$

Here, $V(q) = 4\pi/q^2$ is the Coulomb potential and χ_{ee} is the interacting-electron response function at the electron density n and temperature T_e. To go beyond the random phase approximation (RPA), we use the following finite-T response function:

$$\chi_{ee}(q,n,T_e) = \frac{\chi_0(q,n,T_e)}{1 - V(q)[1 - G(q)]\chi_0(q,n,T_e)}, \quad (4)$$

with χ_0 the finite-T Lindhard function and $G(q) = G(q,T_e)$ a local-field correction (LFC) defined as

$$G(q) = \left(1 - \frac{\gamma_0}{\gamma}\right)\left(\frac{q}{k_{\mathrm{TF}}}\right)^2. \quad (5)$$

In the above, the Thomas-Fermi wave vector $k_{\mathrm{TF}} = \sqrt{6\pi n/E_F}$ is defined by the Fermi energy of the system $E_F = 1/(\alpha r_s)$ where r_s is the electron WS radius and $\alpha = (4/9\pi)^{1/3}$. The finite-T interacting electron compressibility $1/\gamma = n^2\partial^2[nf(r_s,T_e)]/\partial n^2$ is determined from the homogeneous electron gas free energy per electron $f(r_s,T_e)$, as given in Eq. (13), which include a finite-T XC contribution f_{XC}. The noninteracting electron compressibility γ_0 is obtained by setting $f_{\mathrm{XC}} = 0$.

The simplicity of the NPA model rests on decomposing the total charge distribution into a superposition of single-center distributions. If the ion-ion structure factor $S_{ii}(q)$ is known, any total electron charge distribution $n_t(q)$ can always be written as a convolution of the $S_{ii}(q)$ with some effective single-center charge distribution $n(q)$, even for transition metals or systems with resonant levels; but, partitioning the electron contributions from states that extend beyond their WS cells without correctly including the physical interactions is not sufficient. Furthermore, a "simple metal" at one temperature may behave as a "transition metal" at another temperature when a shell of electrons begins to transit to the continuum, and *vice versa*. If the system is of such low density that r_{WS} is larger than the bond length of a possible dimer (e.g., Li$_2$), then the dimer itself will be contained within the WS sphere, and in such cases the NPA model fails; a more elaborate "neutral-pseudomolecule" approach or the use of suitable electron-ion XC potentials $F_{\mathrm{XC}}^{ei}(n,\rho)$ is then needed. We do not examine such nonsimple WDMs in this study. Similarly, at high densities, WDM-Li shows complex phases containing persistent Li$_4$ clusters [38], and the simple NPA model needs modifications. In the present case, a single-center decomposition is physically transparent if the bound-electron core is unambiguously confined within the WS sphere of the ion. We discuss in the results section (Sec. IV D) the variation of the $\bar{Z}$ of Na which changes from unity at low T to 1.49 by $T = 8$ eV. The occupation number in the $2p$ level begins to decrease, while its radius slightly decreases, and hence there is no ambiguity in estimating $\bar{Z} = Z - n_b$ where n_b are all the bound electrons compactly contained well inside the WS sphere. That is, the electron density pileup Δn_i can be clearly divided into bound and free parts such that $\Delta n_i = n_b + n_f$.

Once this division is achieved, the interaction of an electron with the nucleus plus its core can in most cases be replaced by a pseudopotential U_{ei} which is a weak scatterer because it is constructed using linear response; this is given by

$$U_{ei}(q) = n_f(q)/\chi_{ee}(q,r_s,T_e), \qquad (6)$$

where χ_{ee} is provided by Eq. (4).

Even though linear response is used, the resulting pseudopotential includes nonlinear effects since $n_f(q)$ is the fully nonlinear free-electron density obtained from DFT. Only a range of q between zero to slightly above $2k_F$ (depending on T_e) needs to be included as the large-q behavior (short range in r, i.e., inside the core) is not relevant. The resulting pseudopotential is valid only if it satisfies the relation $U_{ei}/[-\bar{Z}V(q)] \leqslant 1$. Unlike the pseudopotentials used in VASP, ABINIT, and similar DFT codes, this linear-response pseudopotential does not require solving a Schrödinger equation. It is a state-dependent *local* pseudopotential that can be fitted to, say a Heine-Abarankov form for convenience (see Shaw and Harrison [39]). This has a constant core potential $V_{HA} = D$ for $r < r_c$ and it is Coulomb type, $V_{HA} = -\bar{Z}/r$ for $r > r_c$. However, such a fitting is not needed except to conveniently report the pseudopotential and to quantify the core radius associated with the potential. In our NPA calculations we use the numerical form of $U_{ei}(q)$ directly.

The pseudopotential calculated at T_i can be used to form a $2T$ ion-ion pair potential ($2T$PP) with ions at T_i and electrons at T_e since it is a sum of the direct Coulomb interaction and the indirect interaction via the displaced-electron charge, viz.,

$$U_{ii}(q,T_i,T_e) = -\bar{Z}^2(T_i)V(q) + |U_{ei}(q)|^2 \chi_{ee}(q,T_e). \qquad (7)$$

This procedure is valid because $\bar{Z}$ remains unchanged in UFM since the bound core of electrons remains at the initial ion temperature for times $t < \tau_{ei}$. If T_e is large enough to change $\bar{Z}$, be it for UFM or equilibrium systems, then the pseudopotential has to be recalculated using an NPA calculation at the needed temperature.

At low T_e, the Friedel oscillations in the electron density resulting from the sharp discontinuity at $k = 2k_F$ in $\chi_{ee}(q)$ produce oscillations in the pair potential $U_{ii}(r)$. These lead to multiple minima in the ion-ion energy which contribute to the maxima in $g(r)$. Such physically important features are not found in "Slater-sum" approaches [40] to finite-T potentials, in "Yukawa-screening" models [7,41], or in Gordon-Kim models [42]. Furthermore, the charge densities restricted to the WS sphere used in IS models cannot capture such long-range effects. Our NPA pair potential can be used to study phonons in the system or to generate the ion-ion $g_{ii}(r)$ and corresponding structure factor $S_{ii}(k)$ when necessary. The ion subsystem in a UFM is clamped at $T_i \sim 300$ K when Al, Li, and Na are crystalline metals. Hence, the ion-ion pair distribution function is simply given by the relation

$$g_{ii}(\mathbf{r}) = \frac{1}{4\pi\rho} \sum_{\{i\}} \delta(\mathbf{r} - \mathbf{R}_i). \qquad (8)$$

The summation is over the crystal lattice, permitting a simple computation of the ion contribution to the quasi-free energy and pressure from the $2T$ pair potential.

B. NPA quasithermodynamic relations

The total free energy F of the $2T$ system given by the NPA is

$$F = F_{emb} + F_{cav} + F_{heg} + F_{ion}, \qquad (9)$$

where F_{heg}, F_{emb}, F_{cav}, and F_{ion} are, respectively, the free-energy contribution of the interacting homogeneous electron gas (HEG), the embedding free energy of the NPA into the electron gas, the correction from the cavity, and the ion-ion free energy. The only parameters of this model are the nuclear charge Z, electron temperature T_e, and the HEG density n such that the average ion density $\rho = n/\bar{Z}$, itself determined by the ion temperature T_i. We discuss these four terms below, using Hartrees with $\hbar = m_e = |e| = 1$.

(i) The embedding energy F_{emb} is the difference between the free energy of the electron gas containing the central ion and the unperturbed HEG; thus,

$$F_{emb} = T[n + \Delta n(r)] - T[n] - \int \frac{\bar{Z}}{|\mathbf{r}|} \cdot [\Delta n(\mathbf{r}) + c(\mathbf{r})]d\mathbf{r}$$
$$+ \frac{1}{2} \int \frac{[\Delta n(\mathbf{r}) + c(\mathbf{r})]}{|\mathbf{r} - \mathbf{r}'|} \cdot [\Delta n(\mathbf{r}') + c(\mathbf{r}')]d\mathbf{r}\,d\mathbf{r}', \qquad (10)$$

with $T[n]$ the electron kinetic energy.

(ii) The cavity correction F_{cav} is computed from the total screened Coulomb potential $V(r)$ resulting from the total electron displacement $\Delta n(r)$:

$$V_i^*(\mathbf{r}) = \int \frac{[c(\mathbf{r}') + \Delta n(\mathbf{r}') - \bar{Z}\delta(\mathbf{r}' - R_i)]}{|\mathbf{r} - \mathbf{r}'|}d\mathbf{r}'. \qquad (11)$$

Since each cavity involves a charge deficit $\eta(r) = n - c(r)$, the cavity correction is

$$F_{cav} = -\frac{1}{2} \int \frac{\eta(\mathbf{r}) \cdot [c(\mathbf{r}') - m(\mathbf{r}')]}{|\mathbf{r} - \mathbf{r}'|}d\mathbf{r}\,d\mathbf{r}' \qquad (12)$$
$$+ \int \eta(\mathbf{r}) \cdot V^*(\mathbf{r})d\mathbf{r}.$$

(iii) The free energy of the HEG F_{HEG} is written as

$$F_{HEG} = \bar{Z}f(n,T_e) = \bar{Z}[f_0(n,T_e) + f_{xc}(n,T_e)], \qquad (13)$$

where f_0 and f_{XC} are, respectively, the noninteracting and exchange-correlation free energies per electron at the density n and temperature T_e. To compute f_0, we use the thermodynamic relation $f_0 = \Omega_0/nV + \mu_0$, where Ω_0 and μ_0 are the noninteracting grand potential and the chemical potential, respectively.

We emphasize that the NPA correlation-sphere model uses the noninteracting μ_0 associated with the mean electron density n as required by DFT theory. In IS models, the known matter density defines the Wigner-Seitz cell, and the free electrons are confined in it, and the corresponding μ is determined by an integration within the WS sphere [e.g., see Eq. (1) of Faussurier [43], leading to a value of $\mu \neq \mu_0$. In contrast, the mean electron density n, the nuclear charge Z_n, and the temperature T are the only inputs to the NPA code. The computation outputs the corresponding mean ion density ρ and $\bar{Z} = n/\rho$. A series of calculations are done in a range of n and the specific n which gives the physical ion density, viz.,

ρ is selected. For a given electron density n and temperature T_e, the noninteracting chemical potential μ_0 is obtained by satisfying the relation

$$n = (\sqrt{2}/\pi^2)T_e^{3/2} \, I_{1/2}(\mu_0/T_e), \qquad (14)$$

while, using this μ_0, the noninteracting part of the grand potential is given by

$$\Omega_0/V = (2\sqrt{2}/3\pi^2)T_e^{5/2} \, I_{3/2}(\mu_0/T_e), \qquad (15)$$

with $I_\nu(z)$ the Fermi-Dirac integral of order ν. Note that only the noninteracting chemical potential, viz., μ_0, appears in the DFT-level occupations of the NPA model since DFT theory maps the interacting electrons to a system of noninteracting electrons at the *interacting density* (see also Ref. [32]).

The XC contribution f_{XC} is computed directly from the PDW parametrization at the given r_s and T_e. The total free energy per electron of the interacting HEG is the sum of f_0 and f_{XC}.

(iv) The ion-ion interaction energy is given explicitly by the pairwise summation over the pair potential U_{ii} as defined at Eq. (7):

$$F_{\text{ion}} = \frac{1}{V}\frac{1}{2}\sum_{\{i \neq j\}} U_{ii}(|\mathbf{R}_i - \mathbf{R}_j|), \qquad (16)$$

where the sum is over the positions of the ions in their initial crystal configuration. This is the only term in F that depends explicitly on the ion structure.

Both the cavity correction and the embedding energy involve the ion with its bound core of electrons held at the temperature T_i, while the electrons are at T_e. The numerical results are insensitive to using a simple NPA calculation with even the core at T_e, if the bound-state occupancies (and thus $\bar{Z}$) remain virtually unchanged.

The quasiequilibrium pressure of the system is obtained by the appropriate density derivative of the ion-structure-independent free-energy terms while the structure-dependent ion-ion contribution is given by the virial equation

$$P = n^2 \frac{\partial}{\partial n}(F_{\text{heg}} + F_{\text{emb}} + F_{\text{cav}})$$
$$- \int g_{ii}(\mathbf{r})\left(\frac{3}{r}\frac{\partial}{\partial r} - n^2\frac{\partial}{\partial n}\right)U_{ii}(\mathbf{r})d\mathbf{r}. \qquad (17)$$

The explicit electron-density dependence of the ion-ion pair potential is taken into account in computing the pressure [44]. Analytical results can be obtained for the terms

$$P_{\text{emb}} = -\int \eta(\mathbf{r}) \cdot V^*(\mathbf{r})d\mathbf{r}, \qquad (18)$$

$$P_{\text{cav}} = -\bar{Z}V^*(r_{\text{WS}}), \qquad (19)$$

whereas other derivatives have to be done numerically.

III. RESULTS

We used the NPA model to determine the properties of $2T$-WDM as produced by femtosecond laser pulses interacting with three common metals in their usual solid state, viz., aluminum, lithium, and sodium, with electron densities such that r_s is 2.07, 3.25, and 3.93 a.u., corresponding to $\bar{Z} = 3$, 1,

and 1, respectively. Note that the $\bar{Z}$ for Na deviates from unity for $T > 3$ eV. The ion density is kept constant in the calculations for isochoric sodium. We present the $2T$ ion-ion pair potentials, nonequilibrium phonon dispersion curves, and pressures for varying T_e, while the ions remain cold at $T_i = 0.026$ eV (300 K).

A. Ion-ion pair potentials

The first step within our UFM model is to compute the equilibrium (at room temperature, $T_e = T_i = 0.026$ eV) free-electron density $n_f(q)$ from the NPA calculation. The pseudopotential $U_{ei}(q)$ at $T_e = T_i$ can then be obtained using Eq. (6). This pseudopotential is an atomic property that depends on $\bar{Z}$ and on the core radius given the ionic r_{WS}, which is then used to construct ion-ion pair potentials $U_{ii}(q,T_e)$ at any T_e via Eq. (7). For this, the electron response at $T_e \neq T_i$ is used. This method is simpler and numerically almost indistinguishable from calculating the pseduopotential from a full $2T$-NPA procedure where the core electrons are held frozen at T_i and $n_f(q,T_e)$ is calculated from the Kohn-Sham equation, with $\bar{Z}$ remaining unchanged. The agreement between the two different ways of calculating the $2T$ potentials provides a strong check on our calculations. Furthermore, while pair potentials cannot be easily extracted from *ab initio* calculations, the NPA model provides this physically important quantity.

Examples of NPA ion-ion pair potentials at different temperatures are presented in Fig. 1. At equilibrium or sufficiently low T_e, all three pair potentials display Friedel oscillations as discussed in Sec. II. Hence, it requires many neighbor shells to compute the total pairwise ion-ion interaction energy with sufficient precision. For Li and Na, we used 8 shells whereas 30 shells were necessary for the Al-Al interaction. As T_e increases, the sharp Fermi surface breaks down, the discontinuity in $f(k)$ at $k = k_F$ broadens, and oscillations disappear, yielding purely repulsive Yukawa-screened potentials [41].

B. $2T$ quasiequilibrium phonon spectra

As the electrons get heated, the screening weakens and interionic forces become stronger; hence, there is an interest
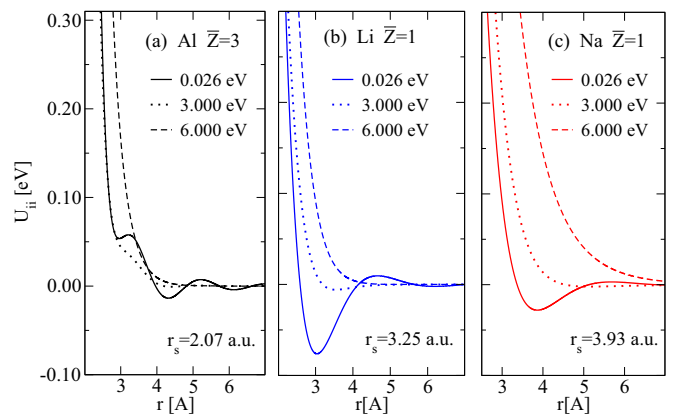

FIG. 1. Two-temperature ion-ion pair potentials for electrons at three different temperatures and ions at $T_i = 0.026$ eV (300 K), for (a) Al, (b) Li, and (c) Na.

in computing the phonon spectra although in many cases the phonon oscillation times may be comparable to the lifetime of the UFM system. Once the $2T$PP is constructed for the desired T_e, the phonon spectra are easily calculated by the diagonalization of the dynamical matrix [45]

$$\mathbf{D}(\mathbf{k}) = \sum_i \mathbf{D}(\mathbf{R}_i) e^{-i\mathbf{k}\cdot\mathbf{R}_i}, \qquad (20)$$

where the elements of the harmonic matrix $\mathbf{D}(\mathbf{R})$ are given by

$$D_{\mu\nu}(\mathbf{R}) = \frac{1}{2} \sum_j \frac{\partial^2 U_{ii}(\mathbf{R}_j)}{\partial u_\mu(\mathbf{R}) \partial u_\nu(\mathbf{0})} \qquad (21)$$

with $\mathbf{R}_j$ the position of the jth atom and U_{ii} the pair potential of Eq. (7). From the s eigenvalues $\lambda_s(\mathbf{k})$ of $\mathbf{D}(\mathbf{k})$, the phonon frequencies are given by $\omega_s(\mathbf{k}) = \sqrt{\lambda_s(\mathbf{k})/M}$ with M the mass of the ion. The resulting phonons are compared with the results from ABINIT-DFT simulations employing density functional perturbation theory [46,47] (DFPT), which determines the second derivative of the energy using the first-order perturbation wave functions. We used the common crystal structure for each metal, i.e., face-centered cubic (fcc) for Al and body-centered cubic (bcc) for Li and Na, with their room temperature lattice parameters $a = 4.05$, 3.49, and 4.23 Å), respectively.

Quasiequilibrium phonon dispersion relations at $T_e = 6$ eV using the two methods are presented in Fig. 2 with the NPA equilibrium phonons as reference to illustrate important modifications in the spectra. In addition, the NPA quasiequilibrium phonon spectrum at $T_e = 12$ eV are also presented; at this temperature DFPT becomes prohibitive. The excellent accord between the NPA and experimental equilibrium phonon spectra at low temperatures has already been demonstrated and shows the meV accuracy of the NPA calculations even at low temperatures [48]. It is not possible to get good accord with experiment in this regime if the free electron density is constrained to be within the Wigner-Seitz sphere, as found by Blenski *et al.* [49] within their ion-sphere model for Al at normal density and at low T.

For the three systems in this study, the two methods (NPA and DFPT) predict very similar $2T$ phonon spectra, thus reconfirming the $2T$ NPA calculations and corroborating the DFPT calculations at finite T. This is important as there are as yet no experimental observations of UFM phonon spectra. In the case of Al, we observe a large increase in frequencies, as high as 32% for longitudinal (L) modes, which supports the "phonon hardening" theory. However, we notice that transverse (T) branches in the $\Gamma - L$ region are barely affected by the electron heating, as was also noted by Recoules [50]. In the case of Li and Na, we find that the spectral modifications are more complex than the "homogeneous" increase found for Al; here, an important increase in the L branch in the middle of the $\Gamma - H$ region takes place, whereas there is no change at the symmetry point H. No modifications to T branches are noticed in this region. In the region $H - \Gamma$, the L-branch frequencies increase in the middle of the region $H - P$ but remain unchanged at the symmetry point H. For the T branch, an increase is noticeable at the maximum in the region $P - \Gamma$ whereas no change affects the minimum in the region $H - P$. In the region $\Gamma - N$ and for the L branch, we
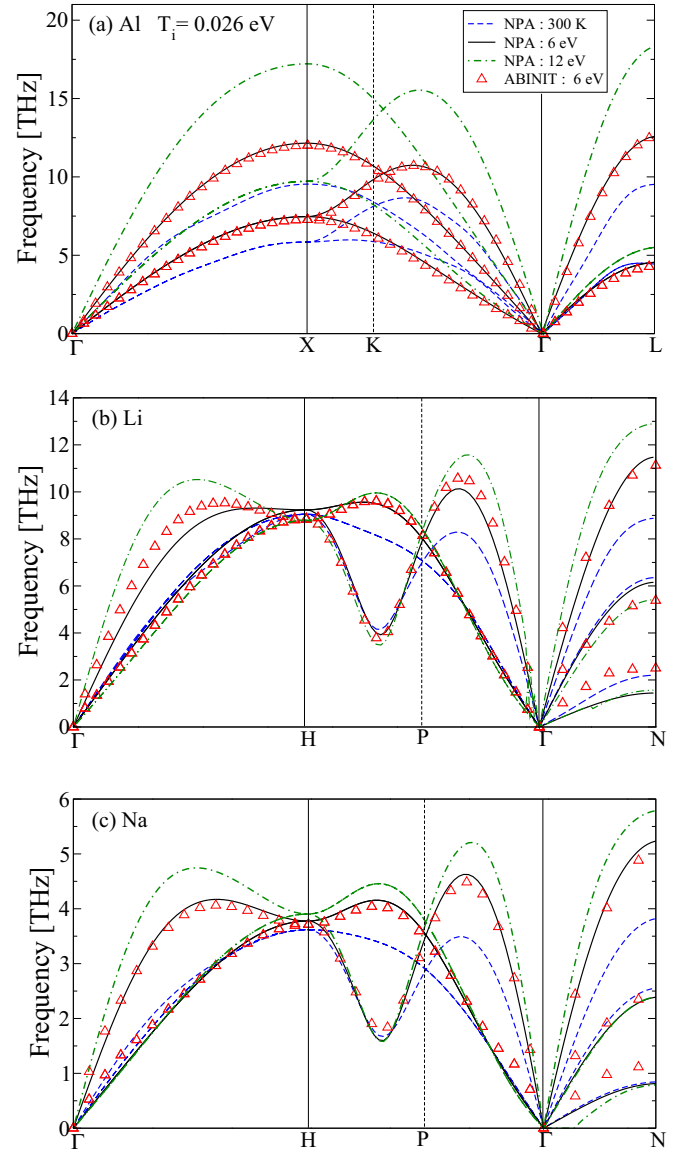

FIG. 2. Quasiequilibrium phonon spectra at $T_e = 6$ eV obtained with NPA and with ABINIT for (a) Al, (b) Li, and (c) Na. The NPA equilibrium phonon spectra at 300 K are shown to illustrate the effect of increasing T_e (dashed lines).

observe the overall largest increase of 29% and 37% for Li and Na, respectively, whereas frequencies of T modes are only slightly modified.

C. $2T$ quasiequilibrium equation of state

A system in its initial equilibrium configuration ($T_i = T_e = T_r$) rapidly reaches a new UFM state with T_i remaining near T_r while T_e increases. However, since the ion motion within the time of arrival of the probe pulse is negligible, the pressure builds up essentially isochorically due to electron heating.

In Fig. 3, we compare the pressure calculated with the NPA model with ABINIT and VASP simulations. In the latter, we used an energy cutoff of 1630 eV for the plane-wave basis, with 60 energy bands to capture finite-T effects. In ABINIT simulations, we used norm-conserving (NC) pseudopotentials with the
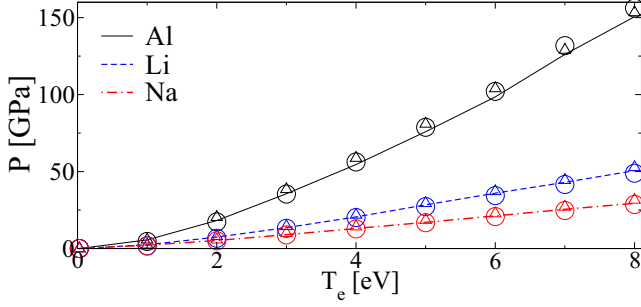
FIG. 3. Quasiequilibrium pressures obtained with the NPA (lines), ABINIT (circles), and VASP (triangles) for Al, Li, and Na.

$T = 0$ Perdew-Burke-Ernzerhof (PBE) XCF within the generalized gradient approximation (GGA). In VASP, we employed projected-augmented-wave (PAW) pseudopotentials with the PBE XCF for Li and Na, and the Perdew-Wang (PW) $T = 0$ XCF for Al. With both codes, pseudopotentials were chosen specifically to simulate $\bar{Z} = 3$ valence electrons for Al, and $\bar{Z} = 1$ for Li and Na as the core electrons remain bound, and at the ion temperature. This is an important aspect discussed in Sec. IV D.

We find that, for all three metals, calculations using NPA, ABINIT, and VASP predict nearly identical pressures with small deviations only at high T_e. At $T_e = 8$ eV, the maximum difference between all models is 9, 4, and 3 GPa for Al, Li, and Na, respectively. Thus, the results from the extension of the NPA model to the $2T$ regime confirms the usability of the solid-state codes at least up to 6 eV on the one hand, and on the the other hand the validity of the NPA approach. However, since NPA uses a finite-T XC functional whereas *ab initio* simulations do not, the effect of such finite-T corrections will be reviewed in Sec. IV.

The computational efficiency and accuracy of the NPA approach make it a valuable tool for studying WDM and other complex systems where iterative computations of materials properties such as $2T$ EOS, $2T$ specific heat, transport properties, opacities, energy-relaxation times, etc., are needed as the system evolves with time since mean ionization, pair potentials, and structure factors are readily obtained. A few minutes on a desktop computer are sufficient in NPA calculations to generate accurate results which require long and intensive computations with DFT+MD.

IV. DISCUSSION

A. Crystal-lattice stability

As electrons absorb the laser energy (within fs time scales) and heat up to T_e, the internal pressure of the system becomes very high as discussed in Sec. III C. In metals, the thermal expansion is also caused by the free-electron pressure. We studied the crystal stability of the solids as a function of lattice expansion; the results are presented in Fig. 4.

For Al at $T_e = 2$ eV, we find that a moderate expansion $a/a_0 = 1.24$ is sufficient to reduce the pressure back to zero, indicating that the crystal may appear stable if the time scale needed for such lattice motion is available before the UFM breaks down. However, in all other cases, the pressure goes
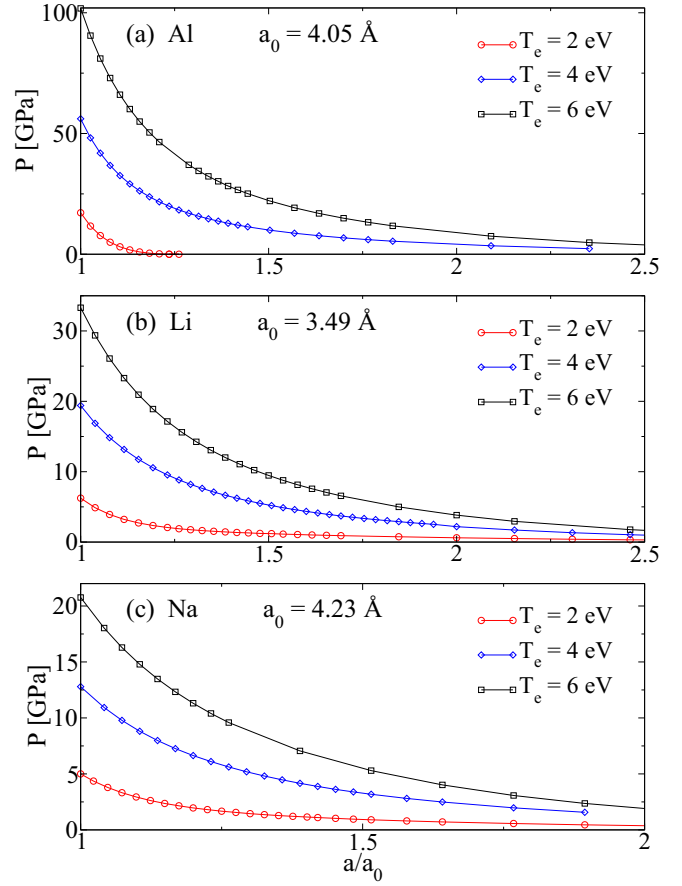

FIG. 4. Total pressure of the solids as a function of the lattice parameter of the crystal relative to the room-temperature value a_0 for (a) Al, (b) Li, and (c) Na.

to zero only asymptotically with increasing lattice parameter, suggesting that such UFM crystals are unstable. Such thermal expansions or spontaneous fluctuations lead to the "explosive" breakdown of the solid on ps time scales. However, since UFM conditions are reached in fs time scales, the ions remain essentially in their initial positions and (as already noted) no net linear forces act upon them due to crystal symmetry. They remain trapped in a stronger harmonic potential leading to hardening of most of the phonon branches. The physical reason for the hardening at increased T_e is the decreased screening of ion-ion interactions by the hotter electron gas.

B. "Phonons" and surface ablation

The UFM system is under very large pressure and the ion-ion $2T$ PP is purely repulsive unless T_e is small (cf. Fig. 1). The discussion in terms of phonons may become inapplicable at higher T_e due to nonzero ablation forces acting on ions in typical UFM samples (0.1–1 μm thick). An ideal periodic lattice implies that the linear derivative of the total potential is zero because the crystal is isochorically constrained by the external pressure. The phonons of UFM "exist" only within this artifice. Small thermal "Debye-Waller"–type ionic displacements u (with a mean value $\langle u \rangle = 0.2$ Å) at 300 K for Al, retained in the UFM) do not render the periodic

TABLE I. The "ablation force" F_{abl} and the "ablation time" τ_{abl} for the (100) surface of an Al slab from VASP and NPA at three different electron temperatures T_e and lattice temperature $T_i = 0.026$ eV. The fastest [100] phonon oscillation time τ_ω is also given for each T_e.

T_e (eV)	F_{abl}^{NPA} (eV/Å)	F_{abl}^{VASP} (eV/Å)	τ_{abl}^{NPA} (fs)	τ_{abl}^{VASP} (fs)	τ_ω (fs)
2.00	0.91	0.90	111	111	105
4.00	2.75	2.70	63.9	64.2	92.6
6.00	5.03	4.70	47.1	48.6	80.6

UFM unstable, and slightly split the degeneracy of transverse branches.

However, pump-probe experiments use very thin metal films. Crystal symmetry is broken and large uncompensated forces act at the surface of the films; as a result, the surface layer and successive layers ablate. We calculated the ablation force F_{abl}^{VASP} on an fcc-(100) Al surface and the two inner layers using the VASP code with the Al surface reconstructed as happens for the cold surface at 0 K. Five layers of Al and five layers of vacuum were used for evaluating the Hellman-Feynman forces on the surface atoms. The NPA method is beyond its regime of validity since the charge density at a surface is not uniform. However, the NPA pressure is the force per unit area at the bounding (100) surface, with one ion per unit area. This is used as the NPA estimate of the ablation force F_{abl}^{NPA}. The forces on the inner neighbor and next-neighbor layers calculated from VASP at $T_e = 6$ eV were 3% and 0.02%, respectively, of the force on the surface layer. The surface force F_{abl} determines an approximate "ablation time" τ_{abl}, the time needed for the surface plane to move by an interplane distance ($a/2$ in the case of Al). This τ_{abl} estimate makes some assumptions, e.g., F_{abl} to be constant over $a/2$, with no movement of inner layers. To verify if phonons can form within such time scales, we compare τ_{abl} with the shortest time for an ion oscillation τ_ω at the highest phonon frequency for the [100] direction; the results are presented in Table I.

As T_e increases, phonons "harden" and F_{abl} increases. In order to observe the "hardening" of phonons on any measurement, a probe time τ_{pr} such that $\tau_\omega < \tau_{pr} < \tau_{abl}$ is required. However, for sufficiently high T_e (e.g., above ∼2 eV for Al), the F_{abl} are strong enough to make $\tau_{abl} < \tau_\omega$. Hence, the ion oscillations have no time to build up and it is probably impossible to satisfy the time constraint enabling the observation of hardened phonons. The phonon concept itself becomes misleading for thin UFM films. Interpreting experiments when $\tau_{pr} > \tau_{abl}$ may require explicit inclusion of surface ablation corrections in the theory used for analyzing optical data (e.g., in the Helmholtz equations).

C. Finite-T exchange and correlation

In the NPA model, we used the finite-T XCF of PDW and assessed the importance of such corrections in the temperature regime studied here. The valence density, or "free" -electron density $n_f(r)$, of the solid at $T_e > T_i$ is the key quantity for the NPA model. In Fig. 5, we present the $n_f(r)$ obtained using the PDW finite-T XCF with that obtained from the zero-T XCF. Even though the correction is small, it may be
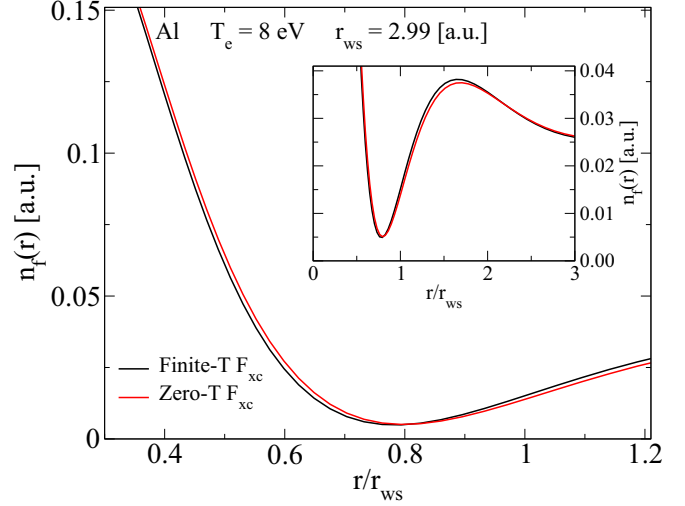

FIG. 5. The NPA free-electron density $n_f(r)$ for Al^{3+} at density $\rho = 2.7$ g/cm³, with $T_e = 8$ eV and $T_i = 0.026$ eV, calculated using XC at finite T and at $T = 0$. The inset shows the density for larger r/r_{ws}.

of importance in some circumstances, e.g., x-ray Thomson scattering spectra, and hence there is no reason to neglect it. The difference between the $T = 0$ XCF and the finite-T XCF increases with $\theta = T/E_F$ at first, and it rapidly and asymptotically goes to zero as $\theta > 1$ and as $T \to \infty$. Hence, the more important consequences of using finite-T XCF should occur in the partially degenerate regime $0 < \theta < 1$.

The finite-T XCF is present in two contributions to the pressure, namely, the electron-electron interacting linear response function $\chi(k, T_e)$, which is used to construct the pseudopotential and the pair potential, and the HEG electron kinetic pressure. Although the finite-T XCF has noticeable effects on the pair potentials or on the energy spectrum of bound states, we observe that overall thermodynamic effects are only slightly sensitive to such finite-T corrections as can be seen in Fig. 6. In fact, at $T_e = 8$ eV, the finite-T XCF only decreases the pressure in Al by 4%. Since individual finite-T contributions are considerable, this insensitivity to XCF comes from the interplay of several terms. For instance, the electron pressure by itself differs by about 10% in the regime $\theta \sim 0.8$,
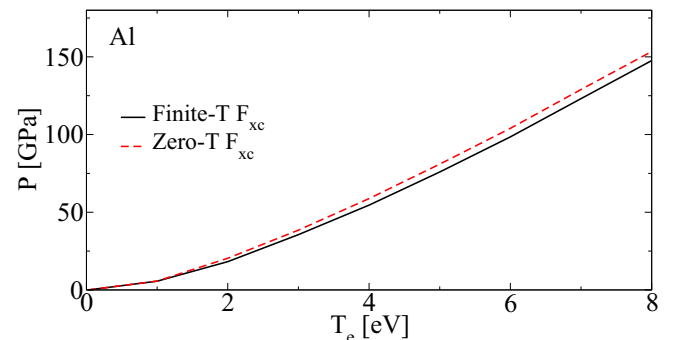

FIG. 6. Comparison between the pressure of Al in the UFM regime computed via the NPA model with the finite-T F_{XC} and with the zero-T F_{XC}.

TABLE II. Mean ionization $\bar{Z}$, the $2p$ Fermi factor, and the $2p$ mean radius (a.u) for sodium (normal solid density) are given as a function of the temperature T in eV. The WS radius $r_{WS} = 3.3912$ a.u. and hence the core is compactly contained inside the WS sphere of Na for all values of T investigated here.

T	$\bar{Z}$	f_{2p}	$\langle r_{2p} \rangle$
1.00	1.001	1.000	0.808
3.00	1.004	0.999	0.804
5.00	1.104	0.983	0.792
8.00	1.494	0.919	0.762
10.0	1.786	0.872	0.744

but the overall pressures obtained from $T = 0$ and finite-T NPA calculations differ by less than 4%.

D. Pseudopotential and mean ionization

Here, we discuss the importance of choosing the proper pseudopotential for *ab initio* simulations of UFM systems in the $2T$ model. The pump-laser frequency is normally chosen such that core electrons are not excited and remain strongly bound to the "cold" nuclei at temperature T_i. Thus, only the $\bar{Z}$ valence electrons on each ion are heated to T_e during the irradiation. In DFT calculations, the electron temperature is used in a Fermi-Dirac distribution for the occupation numbers of all electrons in the simulation. Thus, if the chosen pseudopotential includes more of the core electrons as free electrons, i.e., exceeding the appropriate number of valence electrons, then they too will be "heated" even if they should not be. Then, wrong predictions may result, e.g., for the $2T$ pressure of the given UFM and its electronic specific heat.

To illustrate this point, we carried out ABINIT simulations using PAW pseudopotentials which include $\bar{Z} = 3$ and 9 valence electrons for Li and Na, respectively. We also did NPA-DFT calculations with *all* electrons at T_e. In the NPA model, the mean ionization $\bar{Z} = Z_n - n_b$ can be computed as in Ref. [27]. The $\bar{Z}$ as a function of T_e is not an integer in the NPA but represents an average over different ionization states as discussed in Ref. [14].

In the case of Al and Li, the NPA predicts that $\bar{Z}$ is unaffected for $T_e < 8$ eV, relevant to UFMs. Pressure should also be unchanged, which is exactly what we obtain with the ABINIT simulations of Li using the all-electron PAW pseudopotential. However, in the case of Na, $\bar{Z}$ starts to increase around $T_e = 3$ eV up to $\bar{Z} = 1.49$ at $T_e = 8$ eV (see Table II). The increase in $\bar{Z}$ is accompanied by a decrease in the occupation of the $2p$ level as electrons are promoted to the continuum. The decreased screening in the core (both due to increase of T and due to the decrease in the number of core electrons) leads to a *decrease* in the radius of the $n = 2$ shell. Hence, the increase of $\bar{Z}$ and the modification of the core levels do not lead to any ambiguity in specifying $\bar{Z}$.

We computed the pressure with the NPA model including the changed $\bar{Z}$ and compared it with the ABINIT simulations of Na using the nine-electron PAW pseudopotential. Results are presented in Fig. 7.

We find that, at $T_e = 8$ eV, the pressure, when heating of some core electrons is included, is 54% higher than the
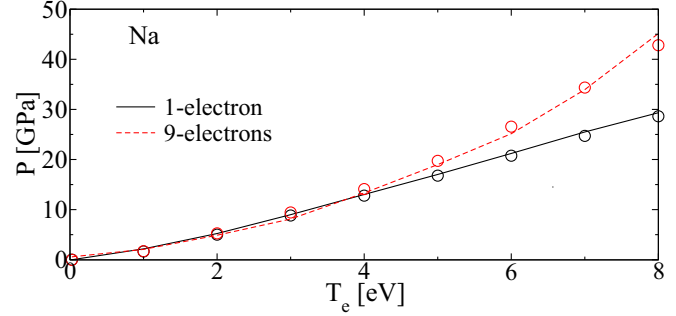

FIG. 7. Comparison between the pressure computed with the NPA (line) and with ABINIT (circles) when heating is applied to the valence electron of Na only or to all electrons (nine electrons in the ABINIT simulations).

correctly calculated value. The use of "all-electron" codes for the study of UFM in the $2T$ state suffers from this pitfall of not selecting the physically appropriate $\bar{Z}$ and the corresponding pseudopotential. When suitable pseudopotentials are not available for DFT+MD calculations, one possibility is to use only the relevant part of the electron density of states (DOS) that is assigned to the free electrons on the basis of $\bar{Z}$, when pressure and related properties are computed. For instance, when calculating the specific heat of "free electrons" for use in UFM studies, the free-electron DOS used in the calculations should be consistent with the number of actual free electrons that couple with the laser. In a metal such as gold (not studied here), even though a pseudopotential with 11 valence electrons is needed, the DOS used for evaluating the electron specific heat for $T_e < 2$ should be only for $\bar{Z} = 1$. The optical properties of gold (see Ref. [51]) show that the d shell couples to light only when the interband threshold energy (~ 2 eV) is exceeded. In the case of gold, the $5d$ shell hybridizes with the continuum electrons (nominally made up of $6s$ electrons) and extends outside the Au-Wigner-Seitz sphere until the $s - d$ transition threshold (~ 2 eV) is reached. Hence, at low temperatures the NPA model with its "one-center" formulation cannot be used for gold at normal density. Similarly, WDM systems with bound states extending outside the Wigner-Seitz sphere cannot be treated unless explicit multicenter electron-ion correlation terms are included.

E. Local pseudopotential for Li

The Li pseudopotential used in the NPA is a *local* pseudopotential, whereas it is widely found in the context of large DFT codes that Li almost always needs a nonlocal pseudopotential. Even in early studies of phonons, a nonlocal pseudopotential was used by Dagens, Rasolt, and Taylor [52], and yet the Li phonons at room temperature they obtained were less satisfactory than for, say, sodium. We have already shown that the NPA pair potential based on a local pseudopotential quite adequately reproduces the Li phonons at room temperature and high temperature at normal density, but not as accurately as for aluminum or sodium. Hence, it is of interest to test the robustness of the Li pseudopotential and pair potential at higher compression by calculating the Li-Li $g(r)$ using the NPA potentials. Here, we use the modified hypernetted chain
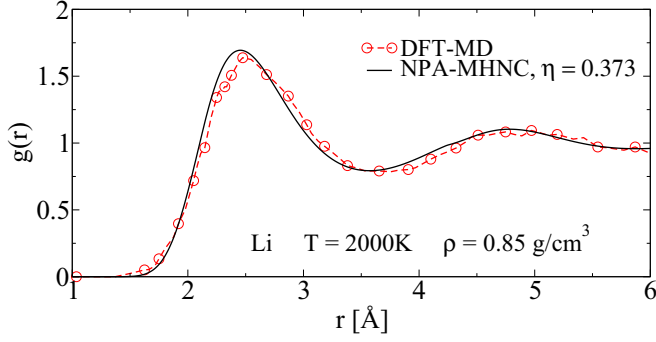
FIG. 8. The Li-Li NPA-MHNC pair distribution function $g(r)$ at 2000 K (0.173 eV), $\rho = 0.85$ g/cm^3, compared with the $g(r)$ of Ref. [54].
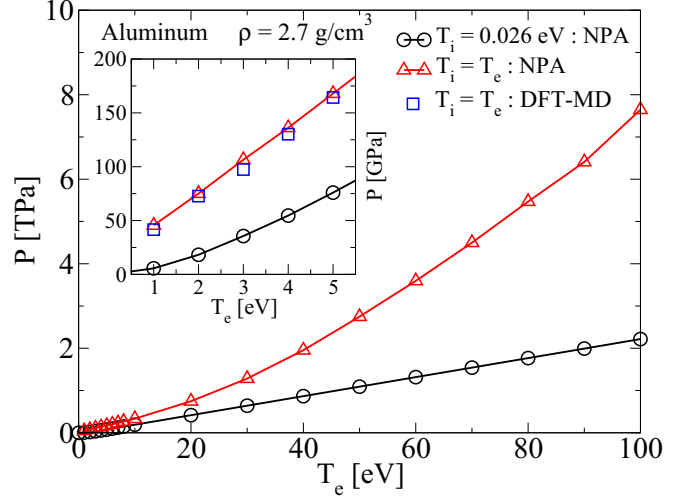

FIG. 9. Comparison of the NPA isochoric pressures for the UFM system and the equilibrium liquid system. Inset: comparison of the NPA pressures in the low-T regime where DFT+MD is practical.

(MHNC) method where a bridge term is included using the Lado-Foiles-Ashcroft (LFA) criterion [53] which is based on the Gibbs-Bogoliubov inequality for the free energy of the system. The MHNC assumes radial symmetry and limits us to "simple-liquid" structures.

Since Li becomes a complex liquid with clustering effects at high compressions [38], we consider a compression of ~1.6 and compute the PDF for Li at 0.85 g/cm^2 and at 2000 K (0.173 eV) for which results are available from Kietzmann *et al.* [54]. The LFA criterion yields a hard-sphere packing fraction $\eta = 0.371$ to model the bridge function. The resulting NPA-MHNC $g(r)$ is displayed together with the $g(r)$ of Ref. [54] in Fig. 8. We find that the simple but state-dependent *local* pseudopotential constructed from the free-electron charge pileup at a Li nucleus is adequate to calculate phonons (i.e, requiring an accuracy of meV energies), as well as the Li-Li PDFs up to moderate compressions and high coupling constants Γ.

F. Comparison between equilibrium WDM and UFM EOS

In UFM, the internal pressure mainly results from the hot electron subsystem since ions remain close to their initial temperature T_r. Here, we investigate the difference in the pressure between the quasiequilibrium UFM regime ($T_i \neq T_e$) and the equilibrium WDM regime which will usually be in a liquid or plasma state with $T_i = T_e$. In DFT codes it is possible to simulate liquids by computing forces among ions and the MD evolution of the positions of the N ions in the simulation cell. However, to obtain reasonable statistics, one needs to use a supercell containing as many ions as possible, thus reducing considerably the first Brillouin zone and increasing the required number of electronic bands to be included. As mentioned earlier, the number of bands needs to be even larger in order to simulate T_e via a Fermi-Dirac distribution. As examples, to obtain reasonably good band occupations for a system of 108 Al atoms at room density, 360 bands at $T_e = 1$ eV are required, and this number grows to 1200 at $T_e = 5$ eV. Thus, since computing repeatedly at every MD step a high number of bands in DFT codes is computationally very demanding, it becomes prohibitive at higher temperatures. Such a problem does not occur in the NPA model as only one DFT calculation at a single nucleus is required to construct the

ion-ion pair potential. The structure factors may be computed using MD, or with MHNC equation for simple liquids.

The comparison of the pressure from UFM and equilibrium WDM is presented in Fig. 9. The equilibrium WDM pressure is much higher than the UFM value. Furthermore, the DFT-NPA calculation is in agreement with NPA up to $T_e = 5$ eV (the limit of our DFT+MD simulation). This mutually reconfirms the validity of the NPA as well as DFT+MD approaches in the WDM regime.

Since $\bar{Z}$ reaches ~7 at $T_e \sim 100$ eV, codes for simulating Al should employ pseudopotentials that include more electrons than the three valence electrons valid at low temperatures. Simulations with high $\bar{Z}$ values will greatly increase the computational load and such calculations become prohibitive. Hence, NPA methods or orbital-free Hohenberg-Kohn methods become relevant [55]. The latter do not, however, provide energy spectra and details of the bound electrons.

V. CONCLUSION

In order to describe physical properties of UFM, we examined applications of the NPA model within the two-temperature quasiequilibrium model. We computed phonons, as well as the pressure resulting from the heating of free electrons. The excellent accord between such NPA calculations and DFT simulations using the ABINIT and VASP codes reconfirms the use of the NPA in this regime. As the internal pressure increases due to the heating of electrons by the ultrafast laser pulses, we explicitly showed that the phonon picture does not have much physical meaning, especially for thin WDM samples, even if frequencies could be computed using the harmonic approximation. As the NPA approach has negligible computational cost compared to standard DFT codes, it is a valuable tool for swiftly and accurately calculating important WDM properties such as mean ionization, pair potentials, structure factors, phonons, x-ray Thomson scattering spectra, electron-ion energy relaxation, conductivity, etc.

[1] G. Dimonte and J. Daligault, Phys. Rev. Lett. **101**, 135001 (2008).

[2] See e.g., V. Mijoule, L. J. Lewis, and M. Meunier, Phys. Rev. A **73**, 033203 (2006).

[3] P. Lorazo, L. J. Lewis, and M. Meunier, Phys. Rev. Lett. **91**, 225502 (2003); Phys. Rev. B **73**, 134108 (2006).

[4] Y. Ping, A. A. Correa, T. Ogitsu, E. Draeger, E. Schwegler, T. Aob, K. Widmanna, D. F. Price, E. Lee, H. Tamb, P. T. Springer, D. Hansonb, I. Koslowb, D. Prendergast, G. Collins, and A. Ng, High Energy Density Phys. **6**, 246 (2010).

[5] H. M. Milchberg, R. R. Freeman, S. C. Davey, and R. M. More, Phys. Rev. Lett. **61**, 2364 (1988).

[6] B. Chimier, V. T. Tikhonchuk, and L. Hallo, Phys. Rev. B **75**, 195124 (2007).

[7] L. Harbour, M. W. C. Dharma-wardana, D. D. Klug, and L. J. Lewis, Phys. Rev. E **94**, 053211 (2016).

[8] K. P. Driver and B. Militzer, Phys. Rev. Lett. **108**, 115502 (2012).

[9] Z. Chen, B. Holst, S. E. Kirkwood, V. Sametoglu, M. Reid, Y. Y. Tsui, V. Recoules, and A. Ng, Phys. Rev. Lett. **110**, 135001 (2013).

[10] N. Medvedev, U. Zastrau, E. Forster, D. O. Gericke, and B. Rethfeld, Phys. Rev. Lett. **107**, 165003 (2011).

[11] L. Dagens, J. Phys. C: Solid State Phys. **5**, 2333 (1972).

[12] L. Dagens, J. Phys. (Paris) **36**, 521 (1975).

[13] N. Garcia, P. Crespo, A. Hernando, C. Bovier, J. Serughetti, and E. Duval, Phys. Rev. B **47**, 570(R) (1993).

[14] F. Perrot and M. W. C. Dharma-wardana, Phys. Rev. E **52**, 5352 (1995).

[15] M. W. C. Dharma-wardana and M. S. Murillo, Phys. Rev. E **77**, 026401 (2008).

[16] M. S. Murillo, J. Weisheit, S. B. Hansen, and M. W. C. Dharma-wardana, Phys. Rev. E **87**, 063113 (2013).

[17] S. H. Glenzer and Ronald Redmer, Rev. Mod. Phys. **81**, 1625 (2009).

[18] P. Hohenberg and W. Kohn, Phys. Rev. **136**, B864 (1964).

[19] W. Kohn and L. J. Sham, Phys. Rev. **140**, A1133 (1965).

[20] F. Perrot, Y. Furutani, and M. W. C. Dharma-wardana, Phys. Rev. A **41**, 1096 (1990).

[21] M. W. C. Dharma-wardana, arXiv:1607.07511.

[22] X. Gonze and C. Lee, Comput. Phys. Commun. **180**, 2582 (2009).

[23] G. Kresse and J. Furthmüller, Phys. Rev. B **54**, 11169 (1996).

[24] F. Perrot and M. W. C. Dharma-wardana, Phys. Rev. A **30**, 2619 (1984).

[25] D. G. Kanhere, P. V. Panat, A. K. Rajagopal, and J. Callaway, Phys. Rev. A **33**, 490 (1986).

[26] H. Iyetomi and S. Ichimaru, Phys. Rev. A **34**, 433 (1986).

[27] F. Perrot and M. W. C. Dharma-wardana, Phys. Rev. B **62**, 16536 (2000); **67**, 079901 (2003).

[28] E. W. Brown, J. L. DuBois, M. Holzmann, and D. M. Ceperley, Phys. Rev. B **88**, 081102(R) (2013).

[29] V. V. Karasiev, T. Sjostrom, J. Dufty, and S. B. Trickey, Phys. Rev. Lett. **112**, 076403 (2014).

[30] M. W. C. Dharma-wardana, Contrib. Plasma Phys. **55**, 79 (2015).

[31] J. M. Ziman, Proc. R. Soc. London **91**, 701 (1967).

[32] M. W. C. Dharma-wardana and F. Perrot, Phys. Rev. A **26**, 2096 (1982).

[33] M. W. C. Dharma-wardana, Phys. Rev. E **86**, 036407 (2012).

[34] M. W. C. Dharma-wardana and F. Perrot, in *Density Functional Theory*, edited by E. H. K. Gross and R. M. Dreizler, NATO ASI Series B: Physics (Plenum, New York, 1993), Vol. 337, pp. 625–650.

[35] S. B. Hansen, A. Y. Faenov, T. A. Pikuz, K. B. Fournier, R. Shepherd, H. Chen, K. Widmann, S. C. Wilks, Y. Ping, H. K. Chung, A. Niles, J. R. Hunter, G. Dyer, and T. Ditmire, Phys. Rev. E **72**, 036408 (2005); B. Wilson *et al.*, J. Quant. Spectrosc. Radiat. Transfer **99**, 658 (2006).

[36] R. Piron and T. Blenski, Phys. Rev. E **83**, 026403 (2011).

[37] C. E. Starrett and D. Saumon, Phys. Rev. E **87**, 013104 (2013).

[38] I. Tamblyn, J.-Y. Raty, and S. A. Bonev, Phys. Rev. Lett. **101**, 075703 (2008).

[39] R. W. Shaw and W. A. Harrison, Phys. Rev. **163**, 604 (1967).

[40] H. Wagenknecht, W. Ebeling, and A. Förster, Contrib. Plasma Phys. **41**, 15 (2001); T. Morita, Prog. Theor. Phys. **20**, 920 (1958).

[41] N. W. Ashcroft and N. D. Mermin, *Solid State Physics* (Saunders College, Philadelphia, 1976), Chap. 17, Eqs. (17.42)–(17-55); A. J. Archer, P. Hopkins, and R. Evans, Phys. Rev. E **74**, 010402(R) (2006).

[42] R. G. Gordon and Y. S. Kim, J. Chem. Phys. **56**, 3122 (1972).

[43] G. Faussurier, Phys. Plasmas **21**, 112707 (2014).

[44] J.-P. Hansen and I. R. McDonald, *Theory of Simple Liquids* (Academic, San Diego, 1990).

[45] N. W. Ashcroft and N. D. Mermin, *Solid State Physics* (Saunders College, Philadelphia, 1976), Chap. 22.

[46] X. Gonze, Phys. Rev. B **55**, 10337 (1997).

[47] X. Gonze and C. Lee, Phys. Rev. B **55**, 10355 (1997).

[48] L. Harbour, M. W. C. Dharma-wardana, D. D. Klug, and L. J. Lewis, Contrib. Plasma. Phys. **55**, 144 (2015).

[49] T. Blenski, R. Piron, C. Caizergues, and B. Cichocki, High Energy Density Phys. **9**, 687 (2013).

[50] V. Recoules, J. Clérouin, G. Zérah, P. M. Anglade, and S. Mazevet, Phys. Rev. Lett. **96**, 055503 (2006).

[51] P. B. Johnson and R. W. Christy, Phys. Rev. B **6**, 4370 (1972).

[52] L. Dagens, M. Rasolt, and R. Taylor, Phys. Rev. B **11**, 2726 (1975).

[53] H. C. Chen and S. K. Lai, Phys. Rev. A **45**, 3831 (1992).

[54] A. Kietzmann, R. Redmer, M. P. Desjarlais, and T. R. Mattsson, Phys. Rev. Lett. **101**, 070401 (2008).

[55] V. V. Karasiev, T. Sjostrom, and S. B. Trickey, Comput. Phys. Commun. **185**, 3240 (2014).